IEEE Photonics Journal
An IEEE Photonics Society Publication

Open Access

Photon Counting Based on Solar-Blind Ultraviolet Intensified Complementary Metal-Oxide-Semiconductor (ICMOS) for Corona Detection

Volume 10, Number 6, December 2018

Yan Wang
Yunsheng Qian
Xiangyu Kong

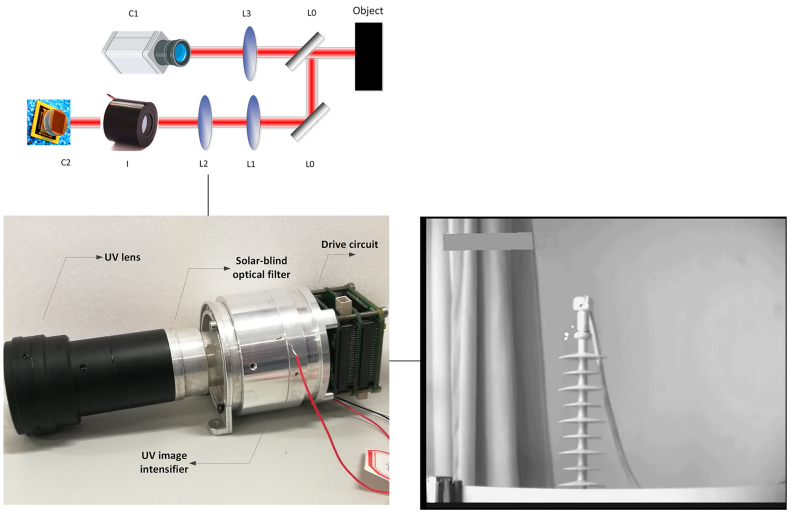

DOI: 10.1109/JPHOT.2018.2876514
1943-0655

IEEE photonics SOCIETY

IEEE

Photon Counting Based on Solar-Blind Ultraviolet Intensified Complementary Metal-Oxide-Semiconductor (ICMOS) for Corona Detection

Yan Wang, Yunsheng Qian, and Xiangyu Kong

School of Electronic Engineering & Photoelectric Technology, Nanjing University of Science & Technology, Nanjing 210094, China

DOI:10.1109/JPHOT.2018.2876514

Manuscript received September 7, 2018; accepted October 13, 2018. Date of publication October 18, 2018; date of current version November 2, 2018. This work was supported by China Postdoctoral Science Foundation under Grant 2017M611813. Corresponding author: Yunsheng Qian (e-mail: yshqian@mail.njust.edu.cn).

Abstract: For the detection of weak signals, photon counting technology has attracted much attention. In this paper, a method based on photon counting is experimentally demonstrated to realize corona discharge detection at solar-blind ultraviolet (UV) wavelength. In our setup, a solar-blind UV optical filter and a Te-Cs cathode are used to eliminate the effects of light with undesired wavelengths, i.e., outside of the solar-blind band. A two-stage microchannel plate with a high voltage can achieve a gain of up to 10^6. A phosphor screen coupled with a CMOS can capture complete images without image distortion. By using an ICMOS, the setup can detect single-photon events. Then, applying photon counting statistics, a theoretical probability model of the photon numbers is obtained. Meanwhile, through analyzing the structure of the photon events considering both pixel and temporal resolution, two photon counting algorithms are proposed. Through experiments with an UV light source, the algorithm based on temporal resolution is proved to be more accurate. Finally, through an experiment with a corona discharge device, a solar-blind photon counting image is captured, and the photon number is calculated through the proposed counting algorithm. The probability curve of the practical photon numbers is acquired via several experiments carried out at the same conditions, which proves the accuracy of the setup and algorithm when compared with the theoretical probability model. Therefore, the proposed method can provide a scientific evaluation for corona detection.

Index Terms: Image analysis, imaging system, photon counting.

1. Introduction

Signal detection under weak illumination has drawn much attention in several fields, ranging from biological sciences to astronomy. In order to detect such low-intensity signals, photon counting technology has been widely applied due to its high sensitivity and low noise [1]–[4]. Various detectors exist for photon counting, such as electron-multiplying charge-coupled device (EMCCD), intensified CCD (ICCD), photo multiplier tube (PMT), single-photon avalanche diode (SPAD) array, and intensified complementary metal–oxide–semiconductor (ICMOS). The traditional detector of photon counting detection is PMT, but it possesses certain disadvantages, including a limited number of independent “pixels” (i.e., spatial resolution), its overall dimensions, and the required high

operating voltages (several kV) [5]–[9]. Both EMCCD and ICCD are array detectors, but their pixels are easily saturated and the spatial resolution is limited [10]–[13]. In recent years, SPAD array and ICMOS have developed rapidly. SPAD array exhibits a fast response with picosecond capabilities [14], but because of process constraints, its pixel size is relatively large, leading to a lower spatial resolution (usually 64 $\times$ 64). Compared with SPAD array, ICMOS, though not as fast, has a wider field and is able to provide a better spatial resolution. Therefore, in this paper, we use ICMOS as the photon counting detector [15].

The spectral range of corona discharge covers the ultraviolet (UV), visible, and infrared bands [16]. In general, the UV band is exploited most frequently for corona detection, since the discovery of UV detection is earlier and the UV detector can function under intense sunlight. The wavelength range of UV corona detection is 200–280 nm, which is often referred to as the solar-blind band. The solar-blind band is mainly absorbed by the ozone layer. Thus, the amount of radiation on the Earth's surface is drastically reduced, reaching a value close to zero. Therefore, solar-blind UV detectors have low background radiation [17]–[21]. However, compared with visible and infrared signals, the UV signal is still weak, reaching single-photon level. Therefore, photon counting detectors are necessary for corona detection. Meanwhile, the number of photons can represent a criterion of the corona discharge degree. At present, the Israeli Ofil firm and U.S. Electric Power Research Institute have co-developed the Octave portable UV imaging device, which can detect coronas, electric arcs and local discharges of high voltage transmission lines and substations. Although the device exists, it exhibits several problems such as blurred corona images and inaccurate number of detected photons.

In this paper, we implemented an experimental ICMOS to realize corona detection based on photon counting. Section 2 described the experimental setup and introduced the realization theory of the photon counting. Photons emitted by a corona were captured by an UV image intensifier. This, coupled with a complementary metal–oxide–semiconductors (CMOS) produced by the New Imaging Technology (NIT) Company, allowed the image of the corona to be acquired and its location to be estimated. Section 3 focused on the applied photon-counting algorithms. Through the analysis of the photon distribution, two photon-counting algorithms based on pixel and temporal resolution were proposed. Based on the counting algorithms proposed in Section 3, Section 4 described the actual experiments and the corresponding results, which can demonstrate the accuracy of the detected number of photon events.

2. Experimental Setup and Theory

The experimental setup is composed of a beam splitting lens, a visible camera, an UV lens, a solar-blind UV optical filter, and a solar-blind UV ICMOS. Fig. 1 depicts the scheme of the experimental setup.

The light from a corona object is incident on the beam splitting lens, which divides it into the visible and UV channels. In this setup, the beam splitting lens can pass all visible light through, and reflect light below 320 nm to the UV channel with the reflectivity of 97%. The visible channel, which detects the relative location of the corona, is composed of a visible lens and a visible camera.

The UV channel consists of an UV lens, an optical filter, an image intensifier, and a CMOS. Firstly, the UV lens focuses on the solar-blind UV object. The quality of the UV lens affects the imaging quality in the UV channel. As we have mentioned before, the solar-blind band means the wavelength between 200–280 nm, but the ordinary optical lens can only focus light signals over 240 nm. Therefore in this paper the sapphire lens with a focus length of 115 mm and a chart size of 1 inch which can focus light signal over 200 nm is adopted to focus the solar blind UV object. Then, the deep cut-off solar-blind optical filter combined with the Te-Cs photocathode is utilized to convert the signal in the solar-blind band to photoelectrons through the photoelectric effect of the cathode. The spectral response curve of the cathode is shown in the Fig. 2. Since the Te-Cs cathode is still responsive over 280 nm, a deep cut-off optical filter is used to eliminate stray light from this waveband, making the input signal of the cathode an effective solar-blind signal. The spectral transmittance (T) and the optical density (OD) of the solar-blind optical filter in this setup

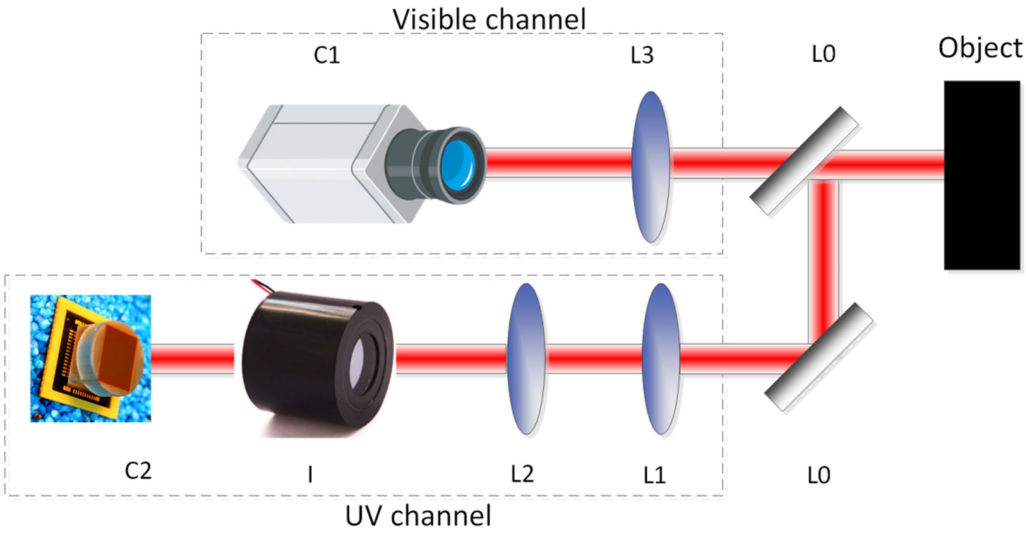

Fig. 1. Experimental setup: C1, visible camera; L3 and L1, visible and UV lens, respectively; L0, beam splitting lens; L2, solar-blind optical filter; I, UV image intensifier; C2, CMOS sensor (NSC1105).

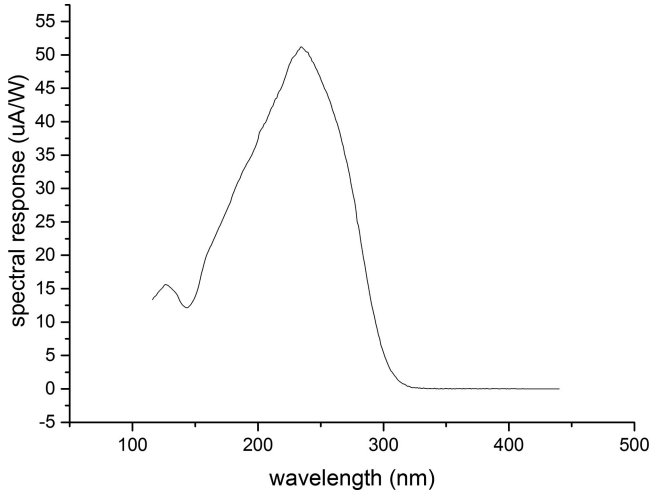

Fig. 2. Spectral response of the Te-Cs cathode in this setup.

are shown in Fig. 3, where $OD = -\log(T)$. By analyzing the curve, the top transmittance is 21.3% at 265 nm, and the transmittance drops rapidly over 280 nm. The OD can reach nearly 12 after 280 nm. Therefore, The phenomena are rather advantageous for solar-blind detection.

Subsequently, the photoelectrons produced by the cathode arrive at the microchannel plate (MCP). In the proposed setup, a two-stage MCP is applied to double the number of photoelectrons. When incident illuminance is below 10^{-5} lx, the detection of light as an analog quantity is made challenging by the limitations of the physics laws. However, detecting light by photon counting is an effective approach. The image intensifier in this setup, using a 2-stage MCP, is ideal for photon counting. When the incident illuminance falls below 10^{-5} lx, the incident photons are separated in time and space. Hence, the photocathode emits very few photoelectrons and only one or no photoelectrons enter each channel of the MCP. Capturing a continuous image with gradation is then no longer possible. In such cases, by applying about 2.4 kV to the 2-stage MCP, increasing its gain to about 10^6, light spots (single-photon spots) with an approximately 60 um diameter corresponding to individual photoelectrons will appear on the output phosphor screen. The gradations of the output

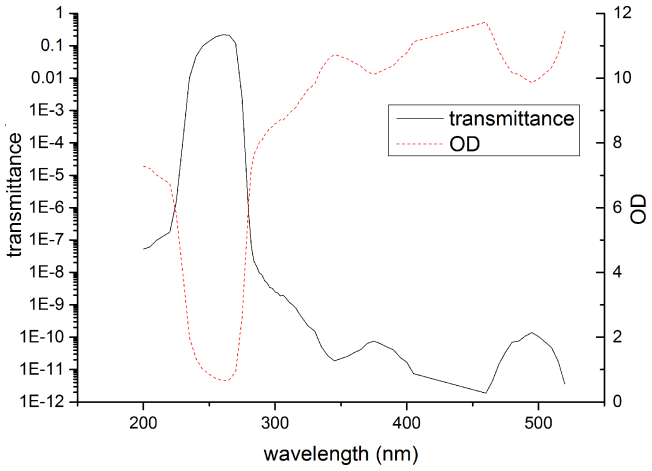

Fig. 3. Spectral transmittance of the optical filter.

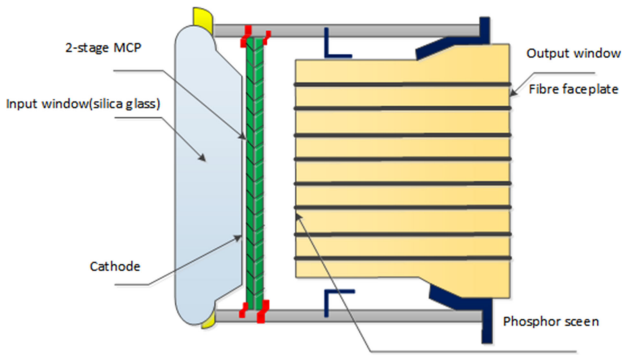

Fig. 4. Structure of the image intensifier.

image are not expressed as a difference in brightness but rather as differences in the time and spatial density distribution of the light spots. Even at extremely low light levels, when only a few light spots appear on the output phosphor screen per second, an image can be obtained by detecting each spot and its position, and integrating them into an image storage unit, such as into a CMOS in the proposed setup. The brightness distribution of this image is configured by the difference in the number of photons at each position. This operation is known as the photon-counting mode. Compared with 1-stage MCP, the gain of 2-stage MCP can increase by three orders of magnitude. Meanwhile, as the gain increases, its noise is greater than 1-stage MCP. For example, the equivalent background input of 1-stage MCP image intensifier is 10^{-5} lx, and the 2-stage MCP image intensifier is 10^{-4} lx. As for the signal-to-noise, although the noise of 2-stage MCP image intensifier is larger than 1-stage MCP, the two image intensifiers are not much different because the signal of 2-stage MCP is much larger than 1-stage MCP. Considering that the solar blind signal is always extremely wake, we utilize the 2-stage MCP image intensifier for its better gain in this paper.

Leaving the MCP, the single photoelectron is amplified to form an electron cloud which bombards the phosphor screen biased to high voltage. As a result, the phosphor screen emits light. The structure of the image intensifier is shown in Fig. 4. At last, the coupled CMOS acquires the light signal emitted by the phosphor screen and transforms it into a digital signal to be analyzed by a computer. The CMOS used in our setup is of the model NSC1105 with a pixel size of 10.6 um $\times$ 10.6 um and a maximum resolution of 1280 $\times$ 1024 produced by the NIT Company. The integral part of the UV channel is shown in Fig. 5.

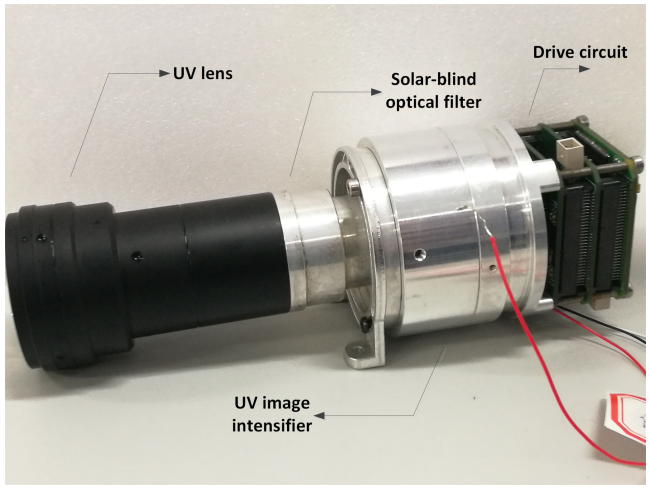

Fig. 5. UV channel of the experimental setup.

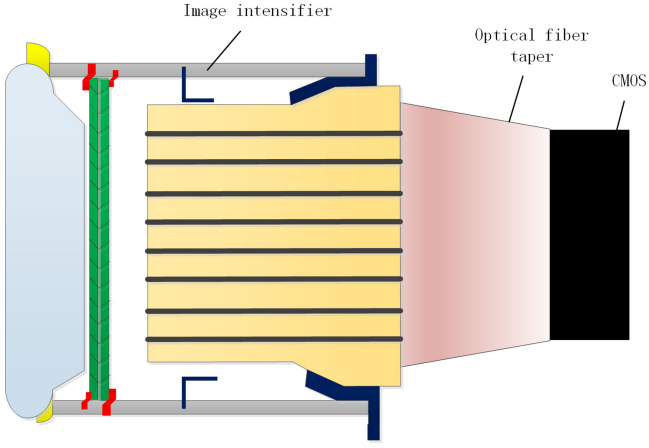

Fig. 6. Schematic diagram of the fiber optic taper.

Considering that the size of the phosphor screen is 18 mm in diameter, a fiber optic taper coupling is usually used for conventional CMOSs due to the size of the CMOSs being smaller than the phosphor screen itself. Fig. 6 shows a schematic diagram of the fiber optic taper. This method reduces the Modulation Transfer Function (MTF) of the image and affects the image quality. Furthermore, the coupling efficiency of the optical fiber taper is 70% in maximum [22]. In this setup, the size of the NSC1105 is 18 mm in diameter, which can be matched by the phosphor screen size. Therefore, it can be directly coupled by the optical fiber. Fig. 7 shows the optical fiber couples to the CMOS. This method results in better MTF and thus, can improve the image quality and the coupling efficiency can be increased to over 90%. Conventional CMOSs have a linear response and are easily saturated. On the contrary, the NSC1105 has a logarithmic response, with a dynamic range of 120 dB, so that the problem of saturation can be resolved. The model of phosphor screen in our setup is P20 and its relative emission spectrum is shown in Fig. 8 (a). From this graph, the highest relative emission intensity is achieved at around 550 nm. The spectral response of the CMOS used in our setup is plotted in Fig. 8 (b), showing that its spectral response is about 80% at around 550 nm. In addition, the response of the CMOS stays above 80% in the entire range of the emission spectrum of the phosphor screen. Therefore, the CMOS can fully absorb the light spots from the phosphor screen.

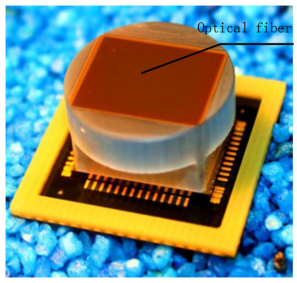

Fig. 7. Optical fiber coupling to the CMOS.

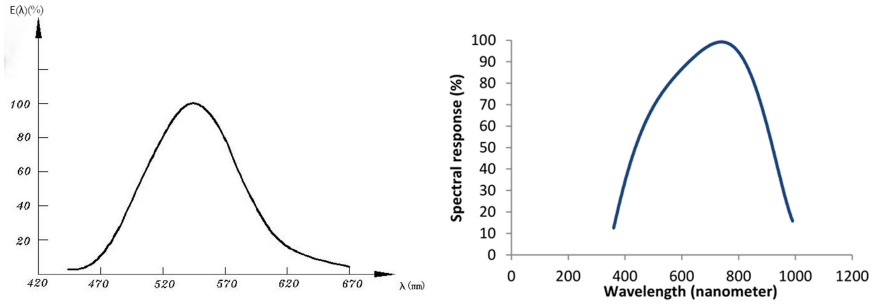

Fig. 8. (a) Relative emission spectrum of phosphor screen; (b) Spectral response curve of the CMOS.

3. Photon Counting

3.1 Photon Counting Statistic

Photon detection follows the Poisson distribution, which is an approximation of the binomial distribution, describing the probability of 'yes' or 'no' outcomes in trials in the limit where the number of possible outcomes becomes large enough for the probability of individual outcomes to become negligible [23].

In photon counting, if the sample emits an average of $\bar{z}$ photons per excitation cycle, according to the Poisson distribution the probability p_n^{ph} that exactly n photons are emitted during one excitation pulse is

$$p_n^{ph} = \frac{\bar{z}^n}{n!} e^{-\bar{z}}. \tag{1}$$

How many of these photons are detected depends on the detector quantum efficiency q. This follows a binomial distribution, leading to the probability of detecting k photoelectrons created by the n photons emitted per excitation cycle

$$p_k = \frac{(q\bar{z})^k}{k!} e^{-q\bar{z}}, \tag{2}$$

and hence the Poisson statistics are preserved.

Since the sum of all probabilities is one, i.e., $\sum_{k=0}^{\infty} p_k = 1$, the number of detected signals N_D is given by the number of excitation pulses N_{rep} multiplied by the probability of detecting the photons:

$$\begin{aligned} N_D &= N_{\text{rep}} \sum_{k=1}^{\infty} p_k = N_{\text{rep}}(1 - p_0) \\ &= N_{\text{rep}}(1 - e^{-q\bar{z}}) = N_{\text{rep}}\left(q\bar{z} - \frac{(q\bar{z})^2}{2!} + \frac{(q\bar{z})^3}{3!} \mp \ldots\right). \end{aligned} \tag{3}$$

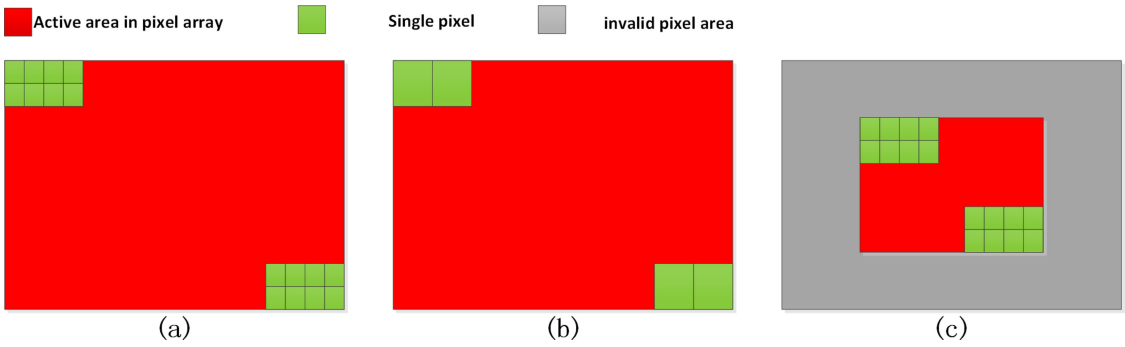

Fig. 9. Schematic diagram for three modes of the NSC1105. (a) HD mode; (b) BIN mode; (c) ZOOM mode.

The average number of detected photons per excitation pulse, α, then can be obtained from the ratio:

$$\alpha = \frac{N_D}{N_{rep}} = 1 - e^{-q\bar{z}} = q\bar{z} - \frac{(q\bar{z})^2}{2!} + \frac{(q\bar{z})^3}{3!} \mp \ldots, \tag{4}$$

i.e., α scales linearly with only when the probability of detecting multiple events after one excitation pulse is negligible. The error in equation (4) is smaller than the first term which is neglected, and it is negligible if it is smaller than other sources of error, e.g., Possion noise which is given by the square root of the number of counts [24].

3.2 High-Frame-Rate Design

Since the afterglow duration of the phosphor screen is generally 6–7 ms in our setup [25], according to the Nyquist sampling frequency requirement, the sampling frame rate of the CMOS needs to be higher than 300 fps in order to be able to carry out accurate photon counting. Based on the features of NSC1105, the CMOS driver is improved to realize a high frame frequency that satisfies the requirements of photon counting.

The CMOS driver mode is selected. The NSC1105 has three driving modes, HD, BIN, and ZOOM, whose schematic diagram is shown in Fig. 9.

The HD mode is characterized by a high resolution, wide field and a low frame frequency. The BIN mode exhibits a low resolution, wide field, and high frame frequency. The ZOOM mode is characterized by a low resolution, narrow field, and high frame frequency. When selected as the mode of CMOS, the BIN mode is used to improve the frame rate and ensure a wider field.

While using the BIN mode, 640 clock ticks are necessary to read out a line of pixels. Considering that the pixel readout time cannot be changed and the internal structure of the CMOS which is shown in Fig. 10, the remaining control signals should be shortened.

Fig. 10 shows that during the data read-out from row *N*, the switches FPN1 and FPN2 open in turn and the integrated optical signal and the dark background signal are exported from the given row of the CMOS. The read-out of both RD1 and RD2 requires at least 1 us, so reading out one row of pixels requires at least 2 us. With the driving frequency of the CMOS being 80 MHz, one row requires 800 cycles to be read out. Meanwhile, the BIN mode requires at least 512 columns in one frame. In addition, to realize the frame rate adjustment, the pixel data is read out in turn after D cycles following the end of RD1 and RD2. Therefore, the row count of the CMOS is $800 + D$, and the column count is 512, and one frame of the CMOS requires $(800 + D) \times 512$ cycle periods. For $D = 0$, the frame rate reaches 195 fps.

After the optimization of the output mode and driving schedule, frame rate of 195 fps can be achieved, which still cannot completely detect the light spots on the phosphor screen. Assuming that image resolution requirement of the CMOS is not too high when used on a solar-blind UV

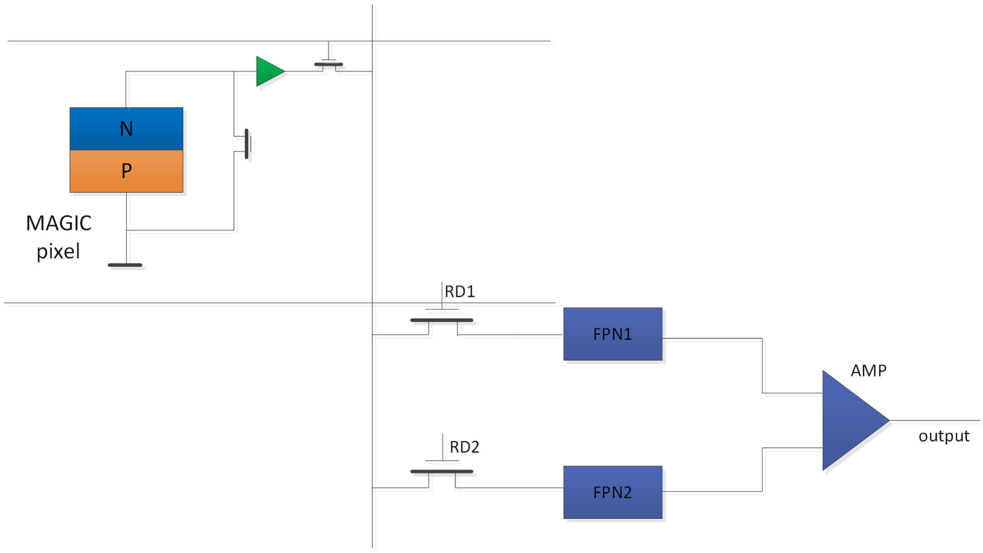

Fig. 10. Internal structure of the CMOS.

target, a significantly higher frame rate can be achieved through sacrificing the image resolution. Therefore, row skipping is applied for driving the CMOS, which means that only the odd-row pixel data is read out while the even-row pixel data is skipped. Subsequently, the image resolution is reduced from 640 $\times$ 480 to 640 $\times$ 240, while the frame rate increases to 390 which is sufficient for recording the afterglow of the phosphor screen.

Fig. 11 shows the CMOS images of a United States Air Force (USAF) 1951 resolution board test chart at varying frame rates proving that the CMOS can record with appropriate quality at the frame rates of 25–390. As the frame rate increases, the integration time decreases and the output images continuously darken. However, due to the logarithmic response of the CMOS, the brightness change of the images is not obvious.

3.3 Photon Counting Algorithm

In our setup, the photons hit the photocathode of the image intensifier at first, which subsequently emits photoelectrons. Through multiplication by the MCP, several bright spots can be observed on the phosphor screen. Finally, a digital image can be captured by the CMOS.

According to the structure and principle of ICMOS, there will be a certain diffusion angle present after the photoelectrons are multiplied by the MCP, and a light spot is imaged on the phosphor screen. A connected region spot, adjacent to others, will be detected by the CMOS. Therefore, the traditional algorithm for photon counting, connected components labeling algorithm (CCLA), is used. Its basic principle can be described as two steps.

Firstly, the photon-counting image is scanned according to rows and columns and pixels greater than a selected threshold T are labeled. Then, starting from the first labeled pixel as a base point, the gray level of each adjacent pixel is checked: if it is also labeled, it is marked as a connected region. These two steps are repeated for every labeled pixel and the number of the connected regions is used to represent the photon number. The algorithm is shown schematically in Fig. 12.

However, with the condition that several beams are incident on the image intensifier at once and the light spots on the phosphor screen are overlapped, the photon number calculated by CCLA is smaller than the true value. A simulation of the overlapping photon events is shown in Fig. 13. Therefore, for more incident photons, the counting error grows. In our paper, the centroid algorithm based on pixel resolution (CAPR) is proposed. Fig. 14 (a) shows a picture captured by the ICMOS and Fig. 14 (b) shows its three-dimensional image obtained by a MATLAB simulation. The CMOS

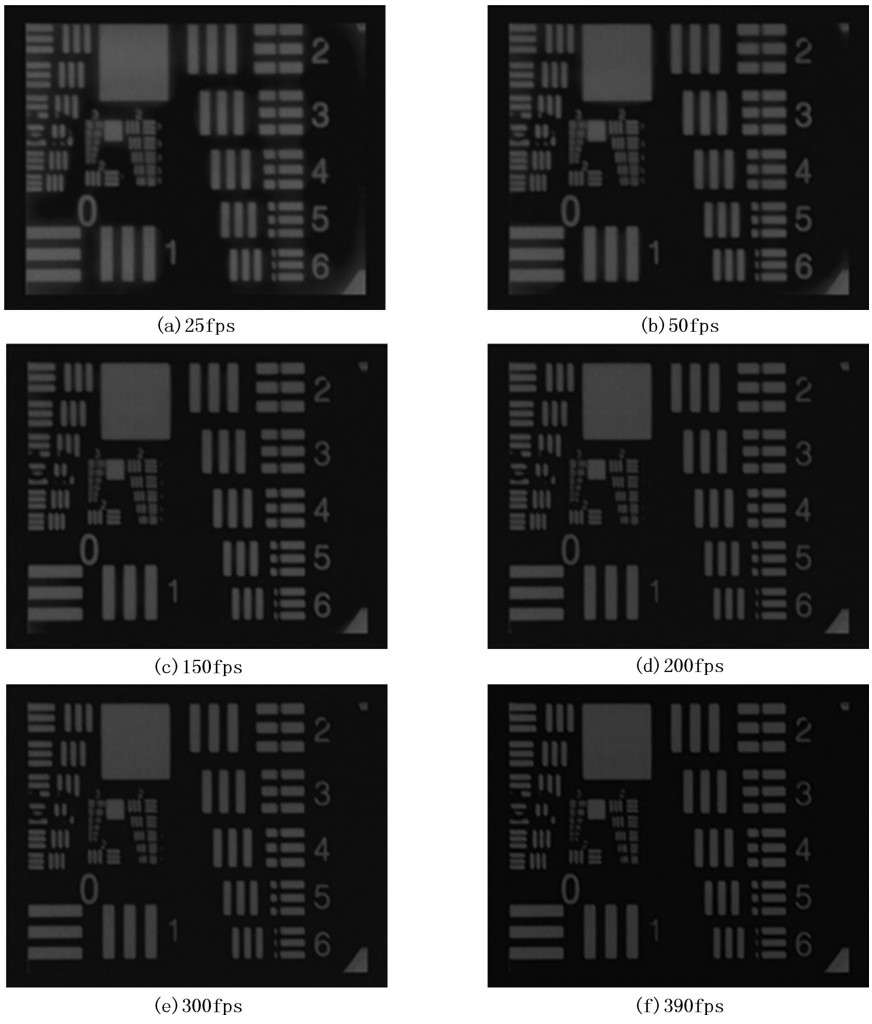

Fig. 11. Images of the USAF1951 resolution board test chart at varying frame rate.

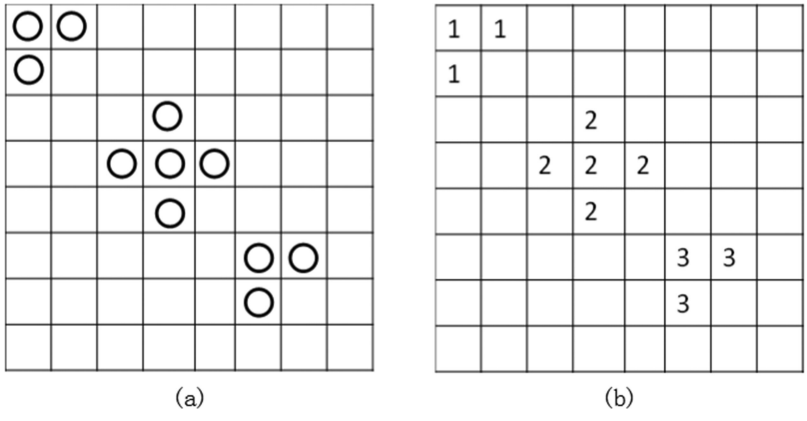

Fig. 12. Basic principle of the connected components labeling method.

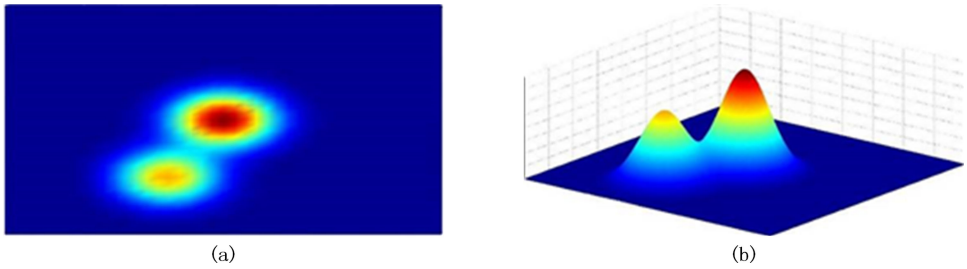

(a) (b)

Fig. 13. Simulation of the overlapping photon events. (a) Top view of the overlapping photon event; (b) side view of the overlapping photon event.

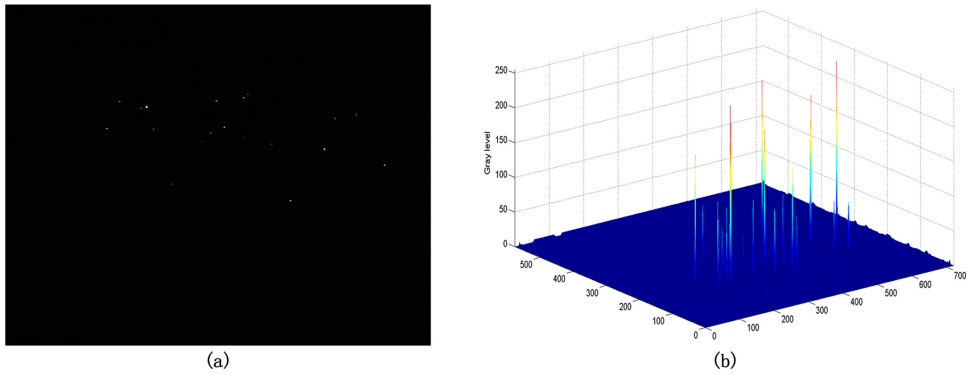

(a) (b)

Fig. 14. (a) Image captured by the ICMOS; (b) Its three-dimensional transformation.

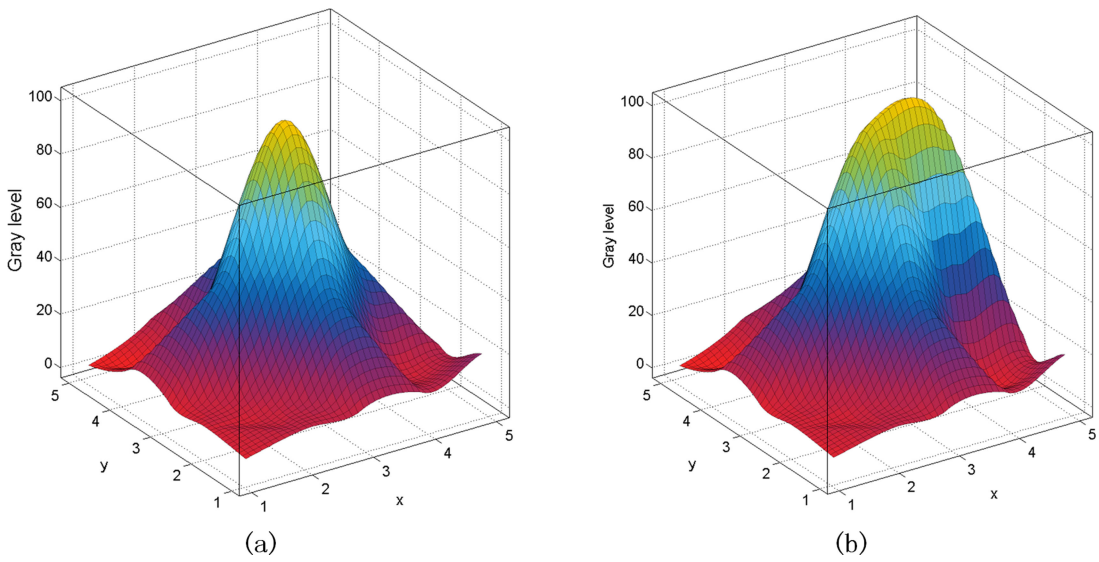

(a) (b)

Fig. 15. (a) Three-dimensional image of a single-photon event; (b) Three dimensional image of a two-photon event.

pixel size in the present work is 10.6 um $\times$ 10.6 um. However, due to the application of the BIN mode and the skipping design, the real pixel size is 21.2 um $\times$ 21.2 um. Through the photon counting mode of the image intensifier, the size of the light spots on the phosphor screen is 60 um in diameter. Hence, we use a 3 $\times$ 3 pixel matrix. The simulation of sample spots is shown in Fig. 15 (a). The subsequent testing principle of the photon events by pixel level analysis is as follows.

Assumed that the coordinate of the image recorded by the ICOMS is (x, y) and the gray level of each pixel is $f(x, y)$. The photon-events image is represented by defocused spots due to the system. Considering the discrete function $f(x, y)$ as a continuous function $g(x, y)$, if the differential function $g'(x_1, y_1) = 0$, as the maximal value of image gray value, (x_1, y_1) can be detected as a photon event. While considering a discrete function $f(x, y)$, its derivative is $f'_x(x, y) = f(x + 1, y) - f(x, y)$, so its local maxima fulfills the following criteria:

$$\begin{cases} f'_x(x, y) > 0 \\ f'_x(x + 1, y) < 0 \\ f'_y(x, y) > 0 \\ f'_y(x, y + 1) < 0 \end{cases} \tag{5}$$

In other words, if $f(x_1, y_1)$ satisfies the above conditions, it can be regarded as a photon event. Meanwhile, when analyzing a vast amount of data, another condition must be met: the maximal value has two consecutive pixels. It is shown by the simulation in Fig. 15 (b). This is because two photons which are incident in two adjacent MCP channels cause the two generated output electrons from each channel to overlap on the phosphor screen. As a result, the peak of this photon event on the phosphor screen is bigger as a consequence of the two photon events interacting with each other. When imaging by the CMOS, these adjacent pixels will exhibit the same maximum value. The condition can be represented as (conditions 1 and 2 are valid for the x dimension, while conditions 3 and 4 for the y dimension)

$$\begin{aligned} condition.1 &\begin{cases} f'_x(x, y) > 0 \\ f'_x(x + 1, y) = 0 \\ f'_y(x, y) > 0 \\ f'_y(x, y + 1) < 0 \end{cases}; \\ condition.2 &\begin{cases} f'_x(x, y) = 0 \\ f'_x(x + 1, y) < 0 \\ f'_y(x, y) > 0 \\ f'_y(x, y + 1) < 0 \end{cases}; \\ condition.3 &\begin{cases} f'_x(x, y) > 0 \\ f'_x(x + 1, y) < 0 \\ f'_y(x, y) > 0 \\ f'_y(x, y + 1) = 0 \end{cases}; \\ condition.4 &\begin{cases} f'_x(x, y) > 0 \\ f'_x(x + 1, y) < 0 \\ f'_y(x, y) = 0 \\ f'_y(x, y + 1) < 0 \end{cases}. \end{aligned} \tag{6}$$

Every pixel (x, y) that satisfies any of conditions 1–4 can be regarded as a photon event. Finally, after checking every pixel in the ICMOS images, the photon number can be obtained by counting the pixels satisfying the above two conditions.

Both methods are based on single-frame images. Considering that the light spots on the phosphor screen are the result of repeated photon incidence in the adjacent frame, we propose a modified algorithm based on the temporal resolution, which is called the centroid algorithm based on temporal resolution (CATR). This photon event can be regarded as the maximum in both space and time. The simulation of this photon event is shown in Fig. 16.

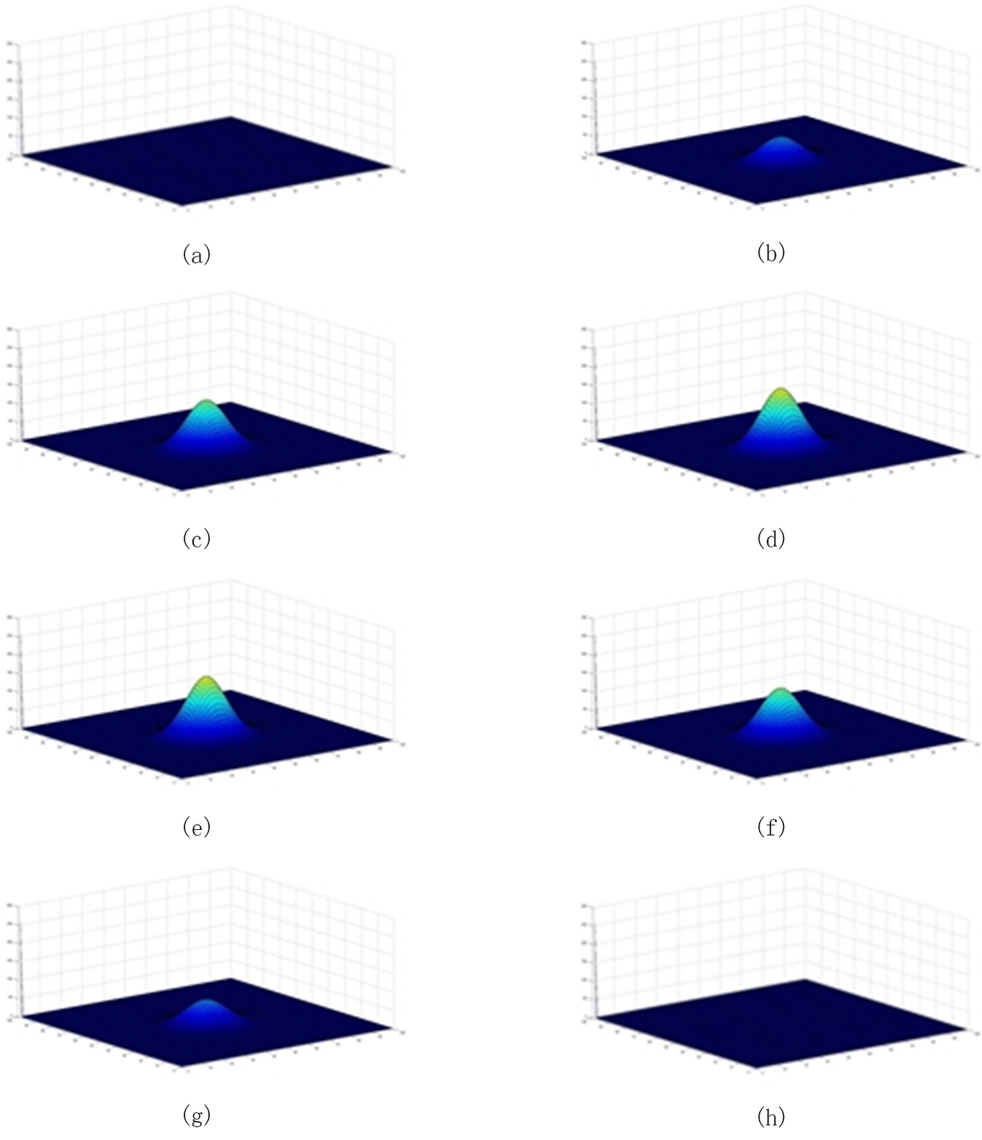

Fig. 16. Simulation of light spots changing over time.

Fig. 16 shows that the light spot on the phosphor screen forms a pulse in time. If several continuous frames can be captured from one pulse, the photon number can be obtained through the comparison of the maximum in a fixed area in those frames.

If the CMOS takes 3 ms per frame, and the duration of one light spot pulse is 6 ms, a total of three continuous frames can be recorded from one light spot pulse, as shown in Fig. 17. Here, a, b, and c correspond to the gray values obtained from the three consecutively frames.

In Fig. 17 (a), the gray value of the middle frame b is the highest, with the values of adjacent two frames being 0. Hence, b can be regarded as the peak of the light spot pulse and it can be recorded as a photon event. In Fig. 17 (b) and (c), the gray value of b is still the highest, but the gray value of one of the adjacent two frames is non-zero, yet smaller than b. At this condition, b can be still considered as a photon event. From the above, as long as the gray value of the middle frame is larger than that of the two adjacent frames, it can be regarded as a photon event. Finally, the number of b that satisfies these conditions in the middle frame is counted as the photon number.

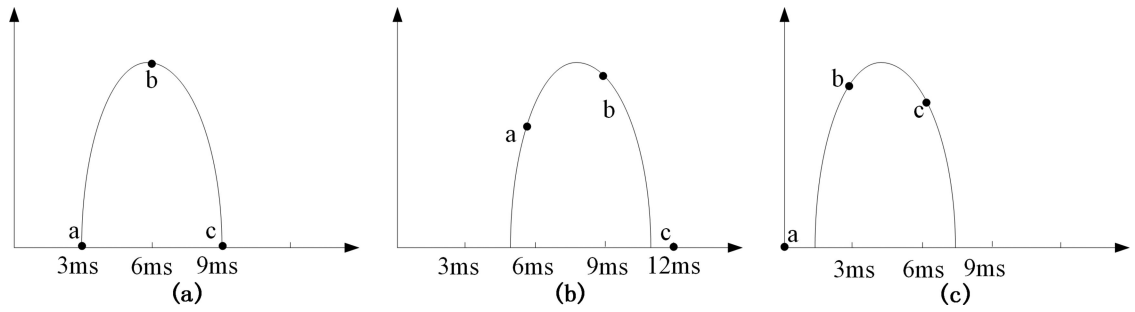

Fig. 17. Sampling of one light spot pulse.

TABLE 1
The Photon Number of Three Dark Count Rate Tests

	Photon number
Test 1	65
Test 2	62
Test 3	70

4. Experimental Analysis

4.1 Experiment of the Dark Count Rate

For the photon counting device, the dark count rate is an important factor to indicate the noise level. It means that in the absence of external photons, the number of photons produced by the setup in 1 second due to internal noise. As the dark count rate is very low and the test fluctuation is large in a short time, it takes a long time to accumulate and average in order to obtain a relatively stable test result. In this experiment, it took 30 seconds for one test and we did three repeated tests totally. Through counting the light spots in the test, the photon number is shown in Table 1. By averaging the photon number obtained, the dark count rate of the setup is 2.2 Hz.

4.2 Experiment With an UV Light Source

We used an UV light source to verify the accuracy of the three photon-counting algorithms mentioned above. The UV light source used in the experiment is a 7ILD30 xenon light source, produced by the Saifan Photoelectric Instrument Company. While detecting under single-photon conditions, the optical power cannot be set clearly, and the intensity of the UV signal is controlled by manually adjusting the aperture mounted on the light source. During the experiments, the voltage of the 2-MCP was fixed to 1800 V, and through adjusting the aperture, three sets of experiments were performed with varying UV signals. In each set of experiments, we captured three consecutive images shown in Fig. 18: (a), (b), and (c) from the first group; (d), (e), and (f) from the second one; (g), (h), and (i) from the last one. As the UV signal is weak and the original image is very dark, we amplified the pixel values of the image to make them easier to watch.

Consequently, through the analysis of the acquired images by MATLAB, considering that CATR needs three consecutive frames, the photon number of the middle frames was calculated based on the three described photon-counting algorithms. The photon number obtained by each counting algorithm is shown in Table 2.

Evaluating these results, for very weak UV signals, the light spot distribution is more dispersed and the results of the three algorithms perform more similarly. As the signal increases, the spots happen to overlap, and the photon number obtained by CCLA does not change substantially.

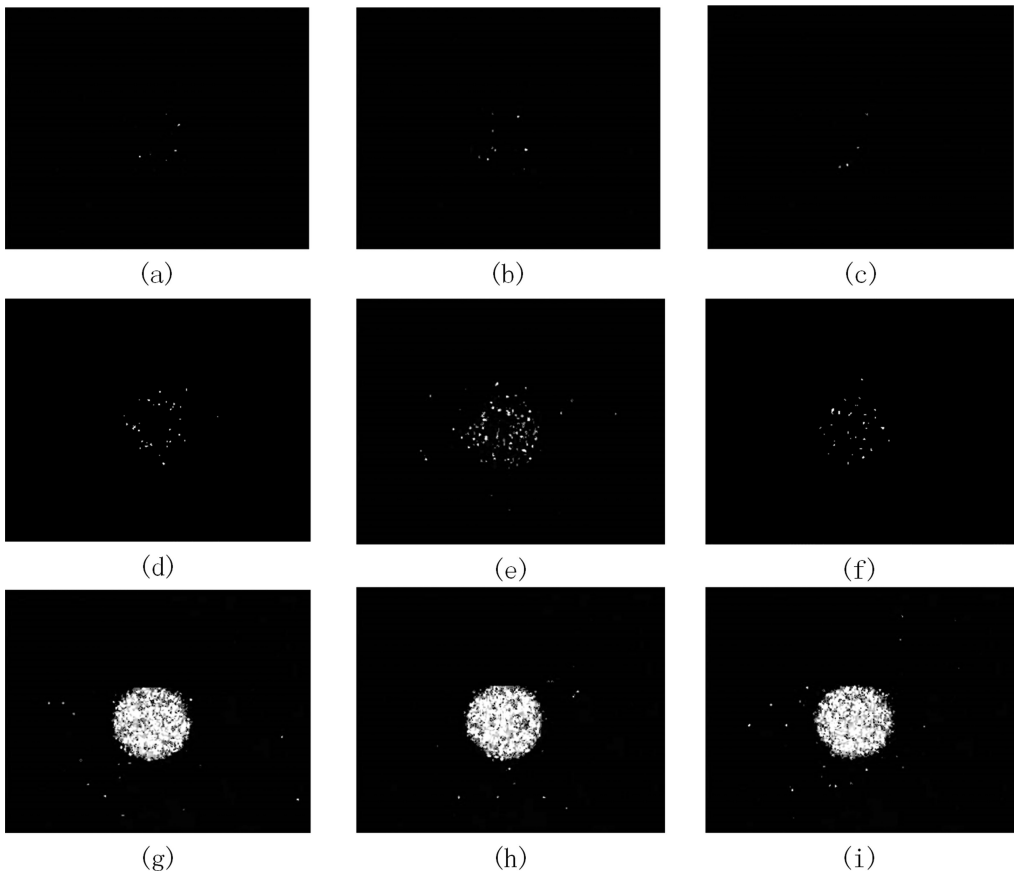

Fig. 18. Three sets of experiments with varying UV signals.

TABLE 2
The Photon Number Obtained by Each Algorithm

	CCLA	CAPR	CATR
Group 1	6	5	5
Group 2	77	83	77
Group 3	87	378	290

Therefore, CCLA is clearly outperformed by CAPR and CATR, as the latter two provide an increasing photon count with the increasing of UV signal. However, the photon numbers obtained by those two algorithms significantly differ. Due to the limitation of the experimental conditions, there is no definite photon number serving as a standard for the UV signal. Hence, further experiments based on the adjustment of the MCP voltage are proposed. Keeping the UV signal unchanged, three additional sets of measurements were completed by setting the MCP voltage to 1500 V, 1800 V and 2100 V. Respectively, three consecutive frames were captured from each set, which are shown in Fig. 19: (a), (b), and (c) from the first set; (d), (e), and (f) from the second one; and (g), (h), and (i) from the last one. As the UV signal is weak and the original image is very dark, we amplified the pixel values of the image to make them easier to watch.

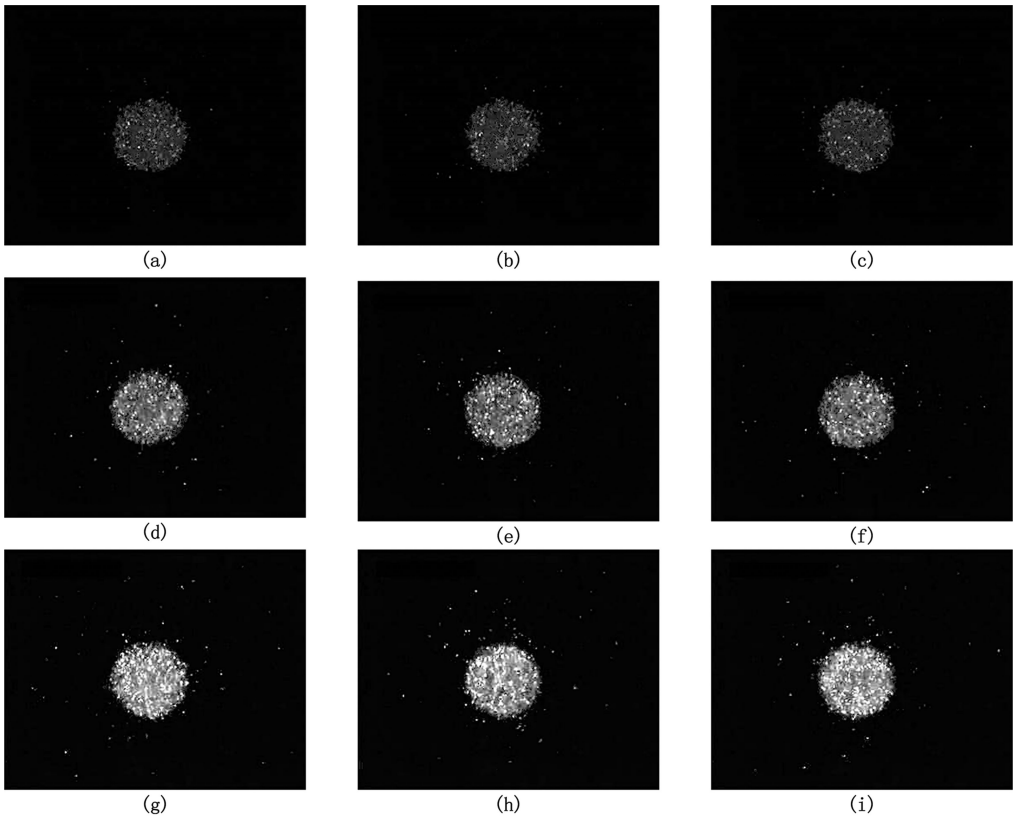

Fig. 19. Three sets of experiments with varying MCP voltages.

TABLE 3
The Photon Numbers Through Adjusting the Voltage on MCP

	CAPR	CATR
Group 1	197	180
Group 2	485	357
Group 3	602	348

The photon numbers calculated by the remaining two algorithms are shown in Table 3 for each set of measurements.

Considering these results, as the MCP voltage increases, the photon count obtained by the CAPR increases continuously. This is a contrast with the UV signal kept unchanged. On the contrary, the CATR provides a photon count that increases firstly and then remains unchanged. This is caused by the insufficient gain of the MCP with an applied the voltage of 1500 V, resulting in an incomplete detection of the UV signal. As the voltage on the MCP increases, the gain reaches a sufficient value to detect the complete UV signal and the photon number in the second and third measurement sets saturates. Therefore, the CATR provides accurate results compared with the other two and can correctly estimate the photon number of the UV signal.

TABLE 4
The Photon Numbers of Repeated Experiments

Group1	Group2	Group3
120	253	357
125	259	368
118	249	360
128	263	370
130	255	365

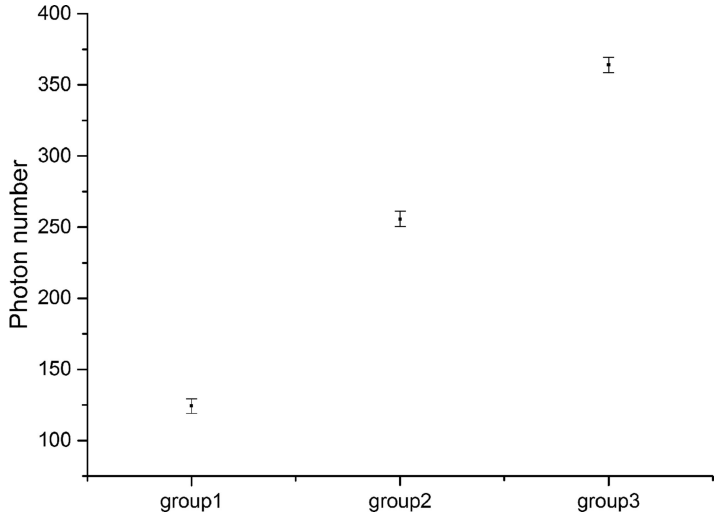

Fig. 20. The error bar of the setup at different UV signal input.

Finally, in order to evaluate the stability of the setup, we fix the voltage of the MCP to 1800 V, and adjust the UV signal inputs to three positions. At each position, five repeated experiments are carried out. The calculated photon numbers by the CATR are shown in Table 4.

Through analyzing these photon numbers, based on the principle of the standard deviation, the error bar on the setup is shown in Fig. 20. Through calculation, the standard deviation at different UV signal input is kept around 5, which can meet the setup stability requirement.

4.3 Experiment of the Imaging Setup

We take an obvious solar-blind source for imaging because the visible and UV channels in the proposed setup require an optical registration to adjust the position of the two channels and the normal corona discharge is too weak to give an accurate direction estimate. In this paper, an alcohol burner is used as the solar-blind target. Fig. 21 shows the final image captured by the setup. The images from the visible camera and the ICMOS are shown in Fig. 21 (a) and (b) respectively, and the final fused image is shown in Fig. 21 (c).

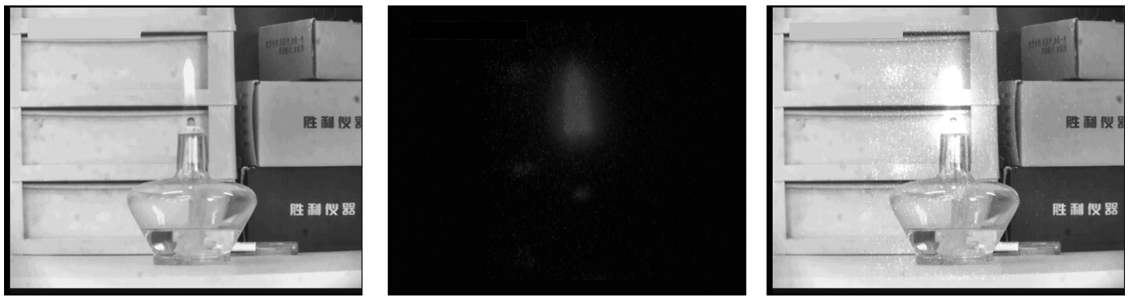

(a) (b) (c)

Fig. 21. Images for the alcohol burner: (a) image of visible camera; (b) image of the UV ICMOS; (c) the fusion image.

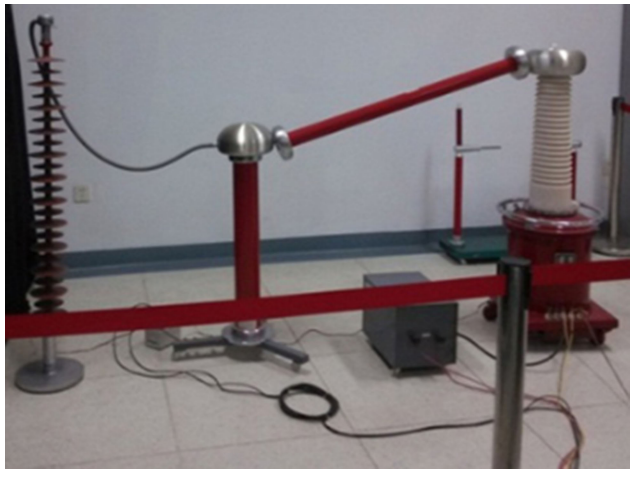

Fig. 22. The partial discharge instrument.

4.4 Experiment With a Corona Discharge and Data Analysis

Through the experiment with the alcohol burner, the setup can be proved to realize imaging in the solar-blind wavelength band. Subsequently, a partial discharge instrument (PDI), shown in Fig. 22, can be used to simulate a corona target. In this experiment, the voltage of the PDI can be adjusted to simulate various intensities of the corona.

Firstly, we set the PDI voltage to 50 kV, 30 kV, and 15 kV respectively. The corresponding fused and UV-channel images are shown in Fig. 23. Through CATR, the corresponding photon numbers are 70, 40, and 27 respectively. As the voltage of the PDI increases, both spot-sizes in the area UV-channel images and the photon numbers get larger. Therefore, the setup can detect the change of intensity of corona discharge.

Consequently, by fixing the voltage of the PDI to 30 kV, we have captured 3600 consecutive frames at a rate of 300 fps. From these, we have counted a total of 1200 photon-number samples. From the data, the obtained photon-number probability curve and the standard Poisson distribution with a parameter of $\lambda = 33$ is shown in Fig. 24. Compared with the Poisson distribution, the obtained probability curve follows the same trend, with its top being in good agreement with the theoretical distribution. From those two curves, it can be concluded that in agreement with the analysis in Section 3.1, as the number of experiments increases, the experimental probability curve approaches the standard Poisson distribution. In addition, the method, including both the setup and the algorithm, proposed in the current work can be proved to be capable of photon counting and by quantification of the corona intensity through photon numbers, it can be used to objectively evaluate corona detection.

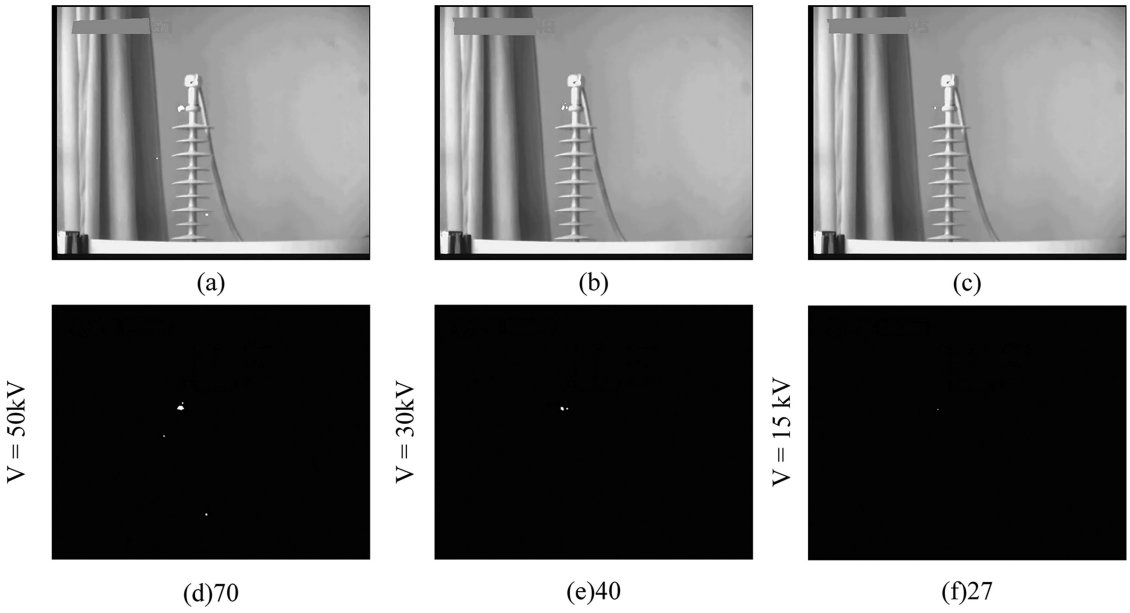

Fig. 23. Results at varying voltages of the PDI: (a)–(c) fusion images of the setup at voltages 50 kV, 30 kV, and 15 kV respectively; (d)–(f) UV images of the setup at voltages 50 kV, 30 kV, and 15 kV respectively. The corresponding photon numbers are 70, 40, and 27 respectively.

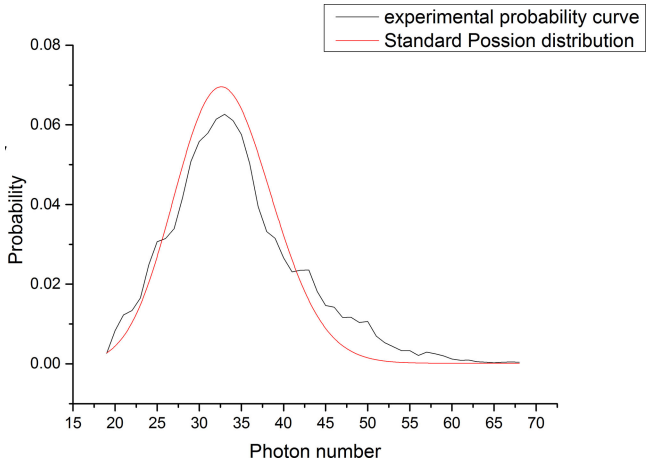

Fig. 24. Comparison of the standard Poisson distribution and the experimental probability curve constructed from 1200 individual photon-counting experiments.

5. Conclusion

In this paper, a corona-detection setup based on solar-blind UV ICOMS was proposed for photon counting. The UV ICMOS can achieve single-photon detection. The utilized two-stage MCP has an enough gain, sufficient for the proposed application. Coupling the phosphor screen to the CMOS sensor through an optical fiber resulted in better image quality and facilitated the capture of complete CMOS images. By the subsequent analysis of the photon states, the probability of the photon numbers was proved to satisfy the Poisson distribution. We proposed two photon counting algorithms based on pixel and temporal resolution. Through experiments with an UV light source, the CATR proved to be more accurate. Finally, the experiments with the PDI proved that the setup can achieve single-photon detection. Through several experiments with the PDI, the practical

probability curve of the photon numbers was counted. Therefore, the method, including the setup and the counting algorithm, can be utilized for corona detection and provide its scientific evaluation.

References

[1] Y. Yang, J. Shi, F. Cao, J. Peng, and G. Zeng, "Computational imaging based on time-correlated single-photon-counting technique at low light level," *Appl. Opt.*, vol. 54, pp. 9277–9283, 2015.

[2] Y. Liu, J. Shi, and G. Zeng, "Single-photon-counting polarization ghost imaging," *Appl. Opt.*, vol. 55, pp. 10347–10351, 2016.

[3] J. Postma, J. B. Hutchings, and D. Leahy, "Calibration and performance of the photon-counting detectors for the ultraviolet imagingtelescope (UVIT) of the Astrosat observatory," *Publ. Astron. Soc. Pac.*, vol. 123, pp. 833–843, 2011.

[4] J. Hutchings, "The UVIT telescopes on the Astrosat observatory," *Astrophys. Space Sci.*, vol. 354, pp. 143–146, 2014.

[5] N. Teranishi, "Toward photon counting image sensors," in *Proc. Imag. Appl. Opt., OSA Tech. Dig. (Opt. Soc. Amer.)*, 2011, Paper IMA1.

[6] F. Guerrieri, S. Tisa, A. Tosi, and F. Zappa, "Two-dimensional SPAD imaging camera for photon counting," *IEEE Photon. J.*, vol. 2, no. 5, pp. 759–774, Oct. 2010.

[7] R. H. Hadfield, "Single-photon detectors for optical quantum information applications," *Nature Photon.*, vol. 3, pp. 696–705, 2009.

[8] F. Magalhães, F. M. Araújo, M. V. Correia, M. Abolbashari, and F. Farahi, "Active illumination single-pixel camera based on compressivesensing," *Appl. Opt.*, vol. 50, pp. 405–414, 2011.

[9] Z. Zhang, L. Wu, Y. Zhang, and Y. Zhao, "Method to improve the signal-to-noise ratio of photon-counting chirped amplitude modulation ladar," *Appl. Opt.*, vol. 52, pp. 274–279, 2013.

[10] L. M. Hirvonen, S. Jiggins, N. Sergent, G. Zanda, and K. Suhling, "Photon counting imaging with an electron-bombarded CCD: towards a parallel-processing photoelectronic time-to-amplitude converter," *Rev. Sci. Instrum.*, vol. 85, 2014, Art. no. 123102.

[11] M. S. Robbins and B. J. Hadwen, "The noise performance of electron multiplying charge-coupled devices," *IEEE Trans. Electron Devices*, vol. 50, no. 5, pp. 1227–1232, May 2003.

[12] S. Tisa, A. Tosi, and F. Zappa, "Fully-integrated CMOS single photon counter," *Opt. Exp.*, vol. 15, no. 6, pp. 2873–2887, Mar. 2007.

[13] S. Tisa, F. Guerrieri, and F. Zappa, "Variable-load quenching circuit for single-photon avalanche diodes," *Opt. Exp.*, vol. 16, no. 3, pp. 2232–2244, Feb. 2008.

[14] E. Charbon, "Single-photon imaging in complementary metal oxide semiconductor processes," *Philos. Trans. Roy. Soc. A*, vol. 372, 2014, Art. no. 20130100.

[15] G. C. Holst and T. S. Lomheim, *CMOS/CCD Sensors and Camera Systems*. Bellingham, WA, USA: SPIE, 2007.

[16] F. Yan, Z. Yu, and X. Yu, "Noise analysis and processing of ultraviolet ICCD for corona detection," *Opt. Precis. Eng.*, vol. 14, no. 4, pp. 709–713, 2006.

[17] L. Wu and W. He, "Solar blind UV and visible dual spectral camera," *Opt. Precis. Eng.*, vol. 18, no. 7, pp. 1529–1535, 2010.

[18] W. Baohua, W. Yuanyuan, Z. Xiaoming, and R. Ningjuan, "Research on solar-blind UV optical imaging system," *Proc. SPIE—Int. Soc. Opt. Eng.*, vol. 9449, 2015, paper 94492L.

[19] Y. Chen, F. Huo, and L. Zheng, "Solar-blind ultraviolet optical system design for missile warning," *Proc. SPIE—Int. Soc. Opt. Eng.*, vol. 9521, 2014, part I, paper 95210X.

[20] F. Zhou, G. Zheng, and F. Yan, "Development status and thoughts of space-based uv warning technology," *Spacecraft Recovery Remote Sens.*, vol. 33, no. 6, pp. 39–44, 2012.

[21] H. Lu, T. Bai, and S. Zhong, "Current status and analysis of ultraviolet alarm technology," *Opt. Techn.*, 26, no. 4, pp. 346–320, 2000.

[22] S. Cui *et al.*, "Analysis and test of coupling efficiency of optical vertebra transmitting device," *J. Chin. Opt.*, vol. 5, no. 6, pp. 610–617, 2012.

[23] L. M. Hirvonen and K. Suhling, "Wide-field TCSPC: Methods and applications," *Meas. Sci. Technol.*, vol. 28, 2017, Art. no. 012003.

[24] P. R. Bevington and D. K. Robinson, *Data Reduction and Error Analysis for the Physical Sciences*. New York, NY, USA: McGraw-Hill, 2003.

[25] Y. Qiu, B. Chang, R. Fu, J. Zhang, L. Sun, and Y. Gao, "Research on testing system of phosphor screen for low light image intensifier," *Opt. Techn.*, vol. 34, no. 3, 2008, pp. 473–475.